Exp Fluids (2014) 55:1823
DOI 10.1007/s00348-014-1823-4

RESEARCH ARTICLE

Simultaneous concentration and velocity field measurements in a shock-accelerated mixing layer

Daniel Reese · Jason Oakley · Alonso Navarro-Nunez · David Rothamer · Chris Weber · Riccardo Bonazza

Received: 13 May 2014 / Revised: 30 August 2014 / Accepted: 4 September 2014

Abstract A novel technique to obtain simultaneous velocity and concentration measurements is applied to the Richtmyer–Meshkov instability. After acceleration by a Mach 2.2 shock wave, the interface between the two gases develops into a turbulent mixing layer. A time-separated pair of acetone planar laser-induced fluorescence images are processed to yield concentration and, through application of the Advection-Corrected Correlation Image Velocimetry technique, velocity fields. This is the first application of this technique to shock-accelerated flows. We show that when applied to numerical simulations, this technique reproduces the velocity field to a similar quality as particle image velocimetry. When applied to the turbulent mixing layer of the experiments, information about the Reynolds number and anisotropy of the flow is obtained.

1 Introduction

The Richtmyer–Meshkov instability (RMI) (Richtmyer 1960; Meshkov 1970) occurs when a shock wave passes through the interface between two fluids of different density, causing the growth of perturbations present at the interface. Misalignment of density and pressure gradients results in baroclinic vorticity deposition, leading to interface deformation and mixing of the two fluids. A finite amount of energy is deposited during the shock-interface interaction, and it is the transfer and dissipation of this energy that govern the development of the instability. When a shock wave passes through a broadband interface, a turbulent mixing layer develops at late times and an accurate description of both the concentration and velocity fields is vital to characterizing this mixing zone. An intimate understanding of the RMI is crucial to the success of inertial confinement fusion (ICF) experiments since the RMI contributes to mixing that inhibits efficiency in ICF and limits the energy production needed for ignition (Ma et al. 2013). The RMI also plays an important role in the understanding of astrophysical phenomena, especially supernovae where stellar core elements are seen at earlier-than-predicted times due to RMI mixing (Arnett 2000).

While traditional particle image velocimetry (PIV) methods are often used to obtain velocity fields in fluid flows, implementing these methods simultaneously with scalar imaging is often difficult or in some cases impossible. Even in cases where it is possible to make concurrent PIV and concentration measurements (Prestridge et al. 2000), seeding a flow with particles to perform PIV will inherently have several downsides. Perhaps the two most prominent limitations associated with seeding a fluid flow include the potential for limited flow tracking fidelity and the possible influence of particles on the dynamics of the flow (Vorobieff et al. 2011). To avoid these issues, methods have been developed that allow for velocity field extraction through the correlation of two successive scalar images. These techniques have been applied previously to planetary imaging, vision research, and to some fluid mechanics experiments (Tokumaru and Dimotakis 1995).

D. Reese (✉) · J. Oakley · A. Navarro-Nunez · R. Bonazza
Department of Engineering Physics, University of Wisconsin—Madison, Madison, WI 53706, USA
e-mail: dtreese@wisc.edu

D. Rothamer
Department of Mechanical Engineering, University of Wisconsin—Madison, Madison, WI 53706, USA

C. Weber
Lawrence Livermore National Laboratory, Livermore, CA 94550, USA

Published online: 16 September 2014

In this publication, we apply one of these techniques, Advection-Corrected Correlation Image Velocimetry (ACCIV) (Asay-Davis et al. 2009), to a turbulent mixing layer caused by the RMI. This is the first application of this technique to high-speed, turbulent RMI flows; therefore, we provide the necessary validation by also applying the technique to numerical simulations.

2 Experimental setup

Image pair data were obtained at the Wisconsin Shock Tube Laboratory: a downward-firing, 9.13-m-vertical shock tube comprised of a circular driver section of 47 cm diameter and a square driven section with 25.4 cm sides (Anderson et al. 2000). The two sections are initially separated by a steel diaphragm, which is burst—creating a shock wave—by opening a set of pneumatically controlled fast-acting valves that connect the driver section to a pair of high-pressure boost tanks. In the driven section, a gravitationally stable stagnation plane is created by flowing helium seeded with 6.5 % acetone by volume from the top of the tube and argon from the bottom. The interface is continuously evacuated through slits on the tube wall at the interface location. After the stagnation plane has stabilized, a statistically repeatable, broadband, shear layer initial condition (Weber et al. 2012) is set up by injecting pure argon and the helium–acetone gas mixture through the side wall of the tube at the interface, as shown in Fig. 1.

Once the shear layer initial condition (Atwood number 0.7) has fully developed, a Mach 2.2 planar shock wave propagates downward and impulsively accelerates the interface, creating a turbulent mixing zone. Two 308 nm excimer lasers are employed for planar laser-induced fluorescence (PLIF), and a Lavision Flowmaster camera captures a pair of images of the mixing layer 2.055 and 2.085 ms after the initial shock-interface interaction.

This time separation of images ensures that diffusion effects between helium and argon are small compared with advection in the flow. With a diffusion coefficient for He–Ar of $D_{ab} = 0.35$ cm^2/s and a characteristic diffusion time of $\tau_D = 30$ μs, we find the diffusion length $\delta = 2(\pi D_{ab}\tau_D)^{1/2}$ (Brouillette and Sturtevant 1994) to be 114 μm. This diffusion length represents the largest possible length scale of diffusion effects and is less than the experimental spatial resolution of 144 μm; therefore, these effects remain unresolved and insignificant compared with advection effects.

3 Data processing

After obtaining the raw experimental image pairs, each post-shock image is corrected for non-uniform laser profile,

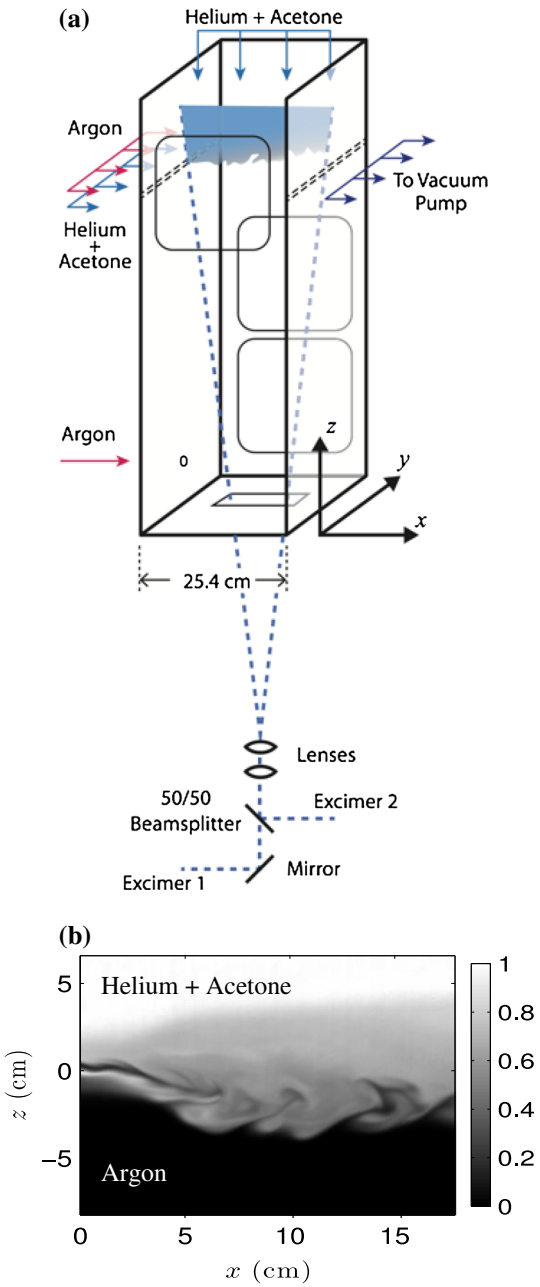

Fig. 1 **a** Experimental setup. **b** Initial condition image corrected to show relative acetone concentration with flow direction from left to right

laser sheet divergence, and Beer's law attenuation, producing images of relative acetone concentration (Weber et al. 2012). The 1D gas dynamics velocity is also subtracted from the second post-shock image to shift the interface up to the same location as in the first post-shock image. This is done to increase the probability that the algorithm will detect a velocity vector and is similar to the technique of displacing the initial interrogation windows in PIV analysis. The actual bulk velocity is recovered and is slightly different from the 1D velocity, as evident by the

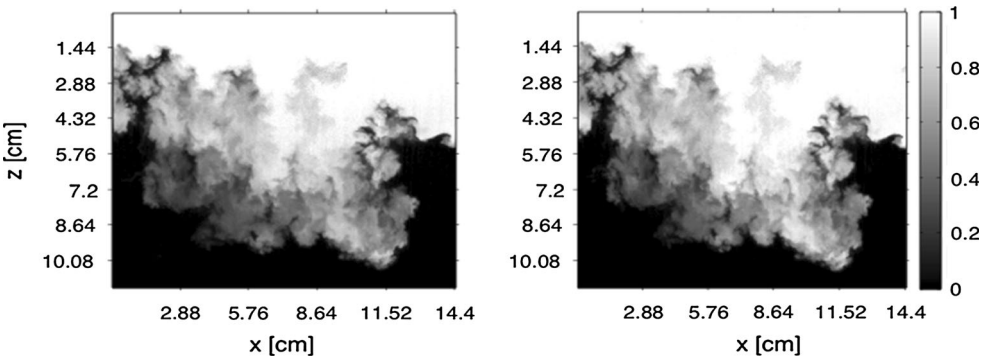

Fig. 2 Sample corrected post-shock image pair

nonzero mean of the streamwise velocity. It is this corrected image pair (see Fig. 2) that is used as input to the ACCIV method, allowing for calculation of the velocity field within the mixing layer.

The ACCIV algorithm is a multi-pass automated correlation image velocimetry (CIV) method originally developed to determine velocity fields in the Jovian atmosphere from scalar images with large time separation (Asay-Davis et al. 2009). ACCIV works by initially finding a box of pixels in the first image that is well correlated with a box of pixels in the second image, from which it calculates a rough estimate of the velocity field. The algorithm will then construct a shear field from this first approximation of velocity and perform a second correlation pass, this time accounting for distortion by shear. ACCIV then uses the full velocity field to both displace and distort the features before applying the two passes in the CIV method. Once this more accurate velocity field has been determined, the correlation search box size can be reduced and iterative improvement of the velocity field can begin.

Four passes of ACCIV were applied to experimental RMI image pairs in order to determine the velocity field within the mixing layer. In each pass, a reduction of the correlation box size, search range, or stride was made. The correlation box size is the size of the box of pixels used to perform correlations, the search range is the range of pixels over which to search for correlations, and the stride is the number of pixels the correlation box is shifted by between correlations. Between each pass, the correlation box size was reduced to between 60 and 83 % of the previous box size, leading to a final correlation box one-third of the original box size. The search range was reduced by 70 % between the first and second ACCIV pass only, while the stride was reduced by one pixel each pass leading to a final stride of one pixel. Typical velocity field results are shown in Fig. 3. Since the flow was not seeded with particulate markers, ACCIV relies on gradients in the scalar images to find correlations between the two images; it leaves patches of no data in regions of constant mole fraction and regions of weak gradients. In a 3 cm × 3 cm region in the center of the mixing layer, velocity data are obtained in approximately 83.3 % of the flow. Comparison with Fig. 2 shows a close correlation of regions of no velocity with pure (white or black) scalar regions.

4 Numerical validation

Before discussing the experimental results in-depth, we first assess the accuracy of ACCIV by applying it to scalar images from a 3D RMI simulation. These simulations matched the spectral content and thickness of the experimental initial condition by using an initial condition defined by the summation of three error functions,

$$\xi(x,y,z) = \frac{1}{2}\left[\frac{1}{3}\left(1 - \mathrm{Erf}\left(\frac{z - z_1 + a_1(x,y)}{d_1}\right)\right) + \frac{1}{3}\left(1 - \mathrm{Erf}\left(\frac{z - z_2 + a_2(x,y)}{d_2}\right)\right) + \frac{1}{3}\left(1 - \mathrm{Erf}\left(\frac{z - z_3 + a_3(x,y)}{d_3}\right)\right)\right]$$

where d1–d3 and z1–z3 were adjusted to match the spanwise-averaged mole fraction profile, the perturbations a1, a2, and a3 were adjusted to match the experiment's spanwise mole fraction variance, and the perturbations were randomly generated using the power-law spectrum of the experimental initial condition (Weber 2012). The simulations were performed using the high-order hydrodynamics code *Miranda* (Cook 2007) and have a spatial resolution of 315 μm. The growth rate of the interface showed convergence at this resolution in similar RMI simulations (Weber et al. 2013; Olson and Greenough 2014).

Despite its similarities with experiment, the simulation was not meant to exactly model the experimental data. Rather, the simulation serves as a means to create a pair of density fields, with a known velocity field between them, containing similar structure and gradient distribution to experimental image pairs (see Fig. 4). In this way, velocity results from ACCIV applied to simulation concentration fields can be directly compared with the known velocity

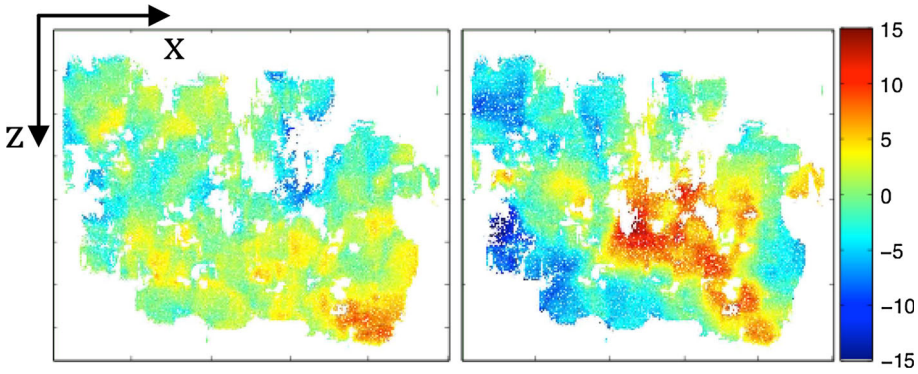

Fig. 3 Sample ACCIV velocity field results in m/s. **a** Transverse velocity field. **b** Streamwise velocity field

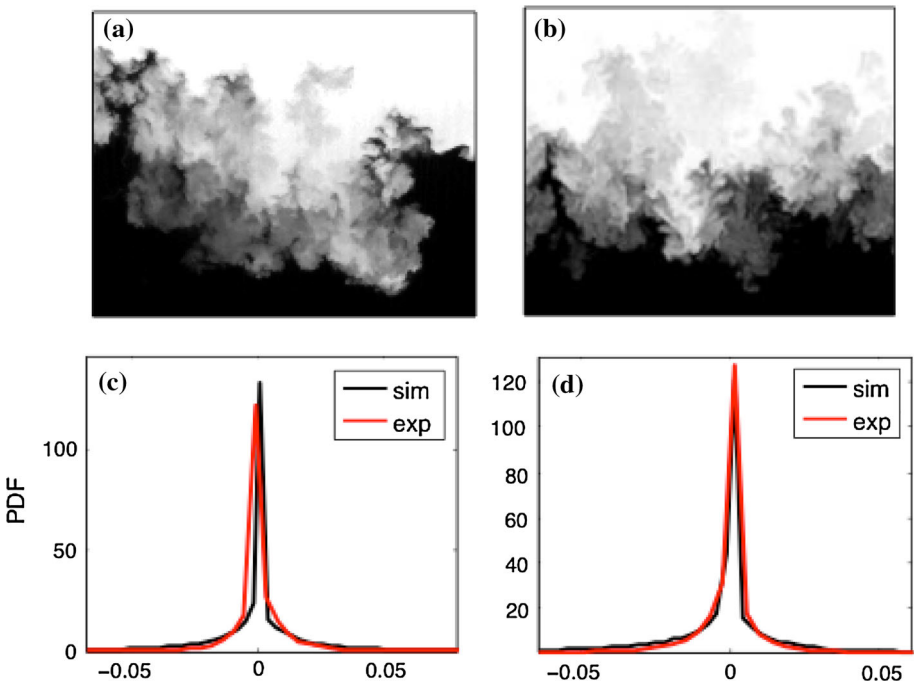

Fig. 4 Comparison of experimental structure and gradient distribution with simulation. **a** Experimental concentration field. **b** Simulation concentration field. **c** PDF of density gradients in transverse direction. **d** PDF of density gradients in streamwise direction

field from the simulation to better understand ACCIV's reliability when applied to a shock-accelerated mixing layer. Because ACCIV can only return velocity values within the mixing layer due to its scalar gradient requirement, a comparison is also made to the simulation velocity field after removing regions where ACCIV is unable to find a velocity vector; this is referred to as the masked simulation result.

In addition to direct comparison with a known velocity field from simulation, results from ACCIV were also compared with traditional PIV results using a synthetic PIV image pair. The PIV images were created by randomly generating an image of Gaussian particles, size 0.5 pixel, for the first image and advecting the particles using the simulation velocity for the second image. The images approximated a typical particle seeding density of 256 particles per 32 × 32 pixel box, a 25 % particle load. Out-of-plane motion and particle inertia were neglected. Unlike ACCIV, PIV methods are not limited by lack of gradients in the scalar field; however, the resolution of PIV velocity field results is dependant on the PIV method used and will often be a fraction of the initial image resolution, though modern PIV techniques are improving on this limitation (Westerweel et al. 2013). For this reason, PIV results were not only directly compared with simulation data and ACCIV, but also with a down-sampled simulation field that matches the resolution of our PIV results.

PIV was carried out using two different software packages: Insight 3G, proprietary software from TSI, and OpenPIV, an open source PIV algorithm (Taylor et al. 2010). For each method, a box size of 8 pixels was employed with a 50 % overlap. The velocity magnitude within the mixing layer is shown in Fig. 5 from various methods. Upon examining each field in Fig. 5, it is seen

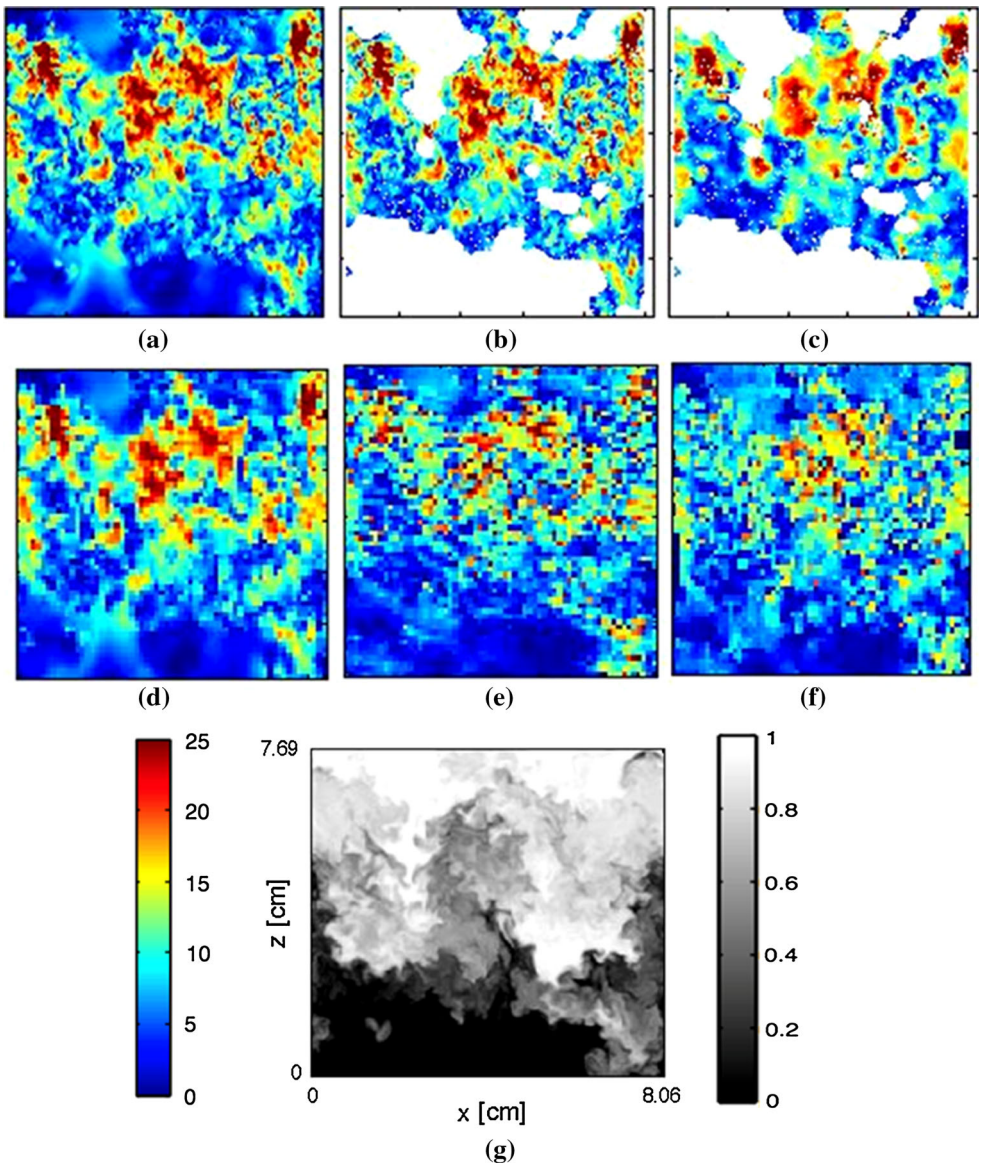

Fig. 5 Velocity magnitude fields in m/s for various methods of velocimetry **a** simulation, **b** masked simulation, **c** ACCIV, **d** down-sampled simulation, **e** OpenPIV, **f** Insight 3G, **g** corresponding scalar field in units of relative acetone concentration

that ACCIV returns higher resolution results than do PIV methods; however, ACCIV only finds velocity vectors in the mixing region, while PIV methods yield full field results. It should be noted that, like ACCIV's dependence on scalar gradients to find velocity vectors, PIV methods rely on particulate markers and will not return vectors where the flow contains an insufficient number of particles. Experimentally, it can be difficult to fully and uniformly seed the entire field of view, so PIV will suffer from intermittency problems in many cases as well.

The probability density functions (PDFs) of each method's streamwise and transverse velocity fields are shown in Fig. 6a, b, respectively. The 1D gas dynamics velocity of 610 m/s has been subtracted off the streamwise component. All methods show close similarities with the simulation's PDFs. ACCIV reproduces the width of the transverse PDF, but fails to capture the magnitude of the PDF peak at zero velocity. Alternatively, Insight 3G most accurately reproduces the PDF peak, but has oscillatory behavior near the half width that does not agree with the simulation.

The standard deviation values and RMS values from these PDFs are reported in Table 1. The ACCIV method produces the closest agreement to the streamwise velocity's standard deviation. In the transverse direction, the Insight 3G PIV method produces better agreement, but the ACCIV method is only larger than the simulations' standard deviation by 13 %. While the ACCIV method fails to reach the peak at near zero velocity that can be seen in the PDFs of simulation and PIV results, we see good agreement between ACCIV and the masked simulation velocity field values. This indicates that most of the zero velocity

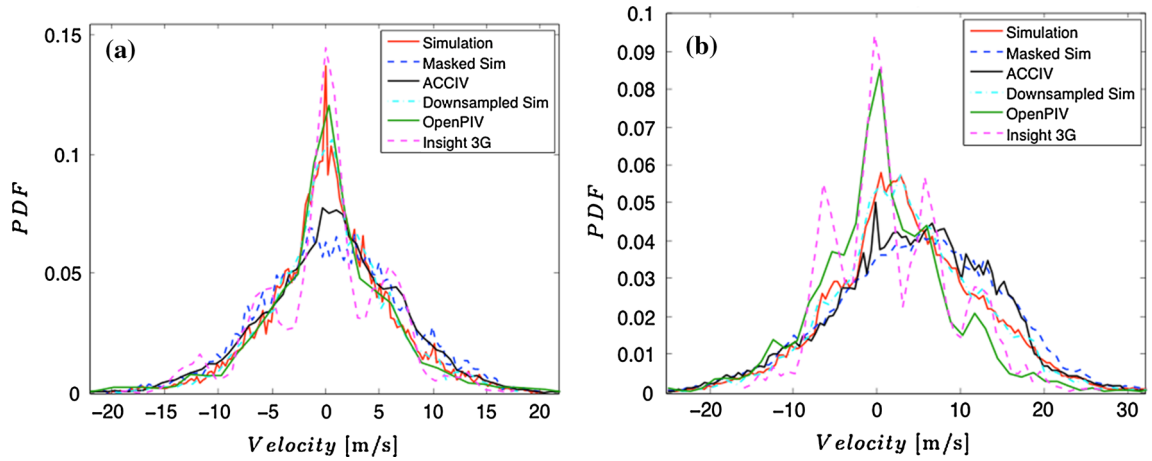

Fig. 6 PDFs of velocity field from simulation. **a** Transverse field. **b** Streamwise field

Table 1 Comparison of RMS values and standard deviation of normal distribution fit (with 95 % confidence intervals) to PDFs of velocity field for each velocimetry method

Method	σ [m/s]	RMS [m/s]
Simulation–stream	8.80 ± 0.05	9.51
Masked sim–stream	9.89 ± 0.07	11.09
Down-sampled–stream	8.47 ± 0.19	9.20
ACCIV–stream	9.30 ± 0.06	10.30
OpenPIV–stream	7.92 ± 0.18	7.94
Insight 3G–stream	7.02 ± 0.16	7.26
Simulation–trans	5.53 ± 0.03	5.55
Masked sim–trans	6.51 ± 0.04	6.53
Down-sampled–trans	5.40 ± 0.12	5.42
ACCIV–Trans	6.27 ± 0.04	6.31
OpenPIV–trans	6.34 ± 0.14	6.34
Insight 3G–trans	5.47 ± 0.12	5.47

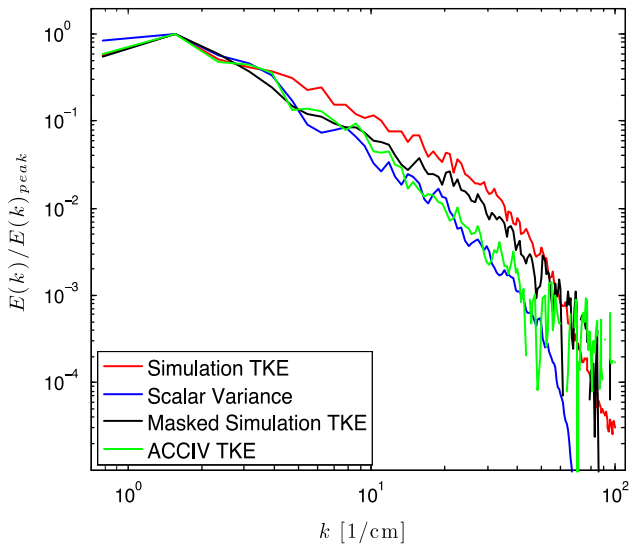

Fig. 7 Planar TKE and scalar variance energy spectra for Simulation and ACCIV data

lies outside the mixing layer, so a majority of the field being masked by ACCIV is near zero velocity. We also see reasonable agreement between PIV and the down-sampled simulation velocity values as was expected due to the loss of resolution associated with performing PIV.

The planar turbulent kinetic energy (TKE) spectrum of the ACCIV velocity field results were also directly compared with the simulation planar TKE and the masked simulation planar TKE spectra. These spectra are then normalized by their peak value and plotted with the scalar variance energy spectrum of the post-shock images (also normalized by its peak value) for comparison as shown in Fig. 7. While reasonable agreement is seen between ACCIV and the simulation, the ACCIV planar TKE spectrum has a slope much closer to that of the scalar variance than one might expect from the masked simulation spectrum. We also notice more noise introduced at the highest wavenumbers for ACCIV results than is seen for the masked simulation spectrum.

5 Experimental results

With the substantiation of ACCIV as a viable PIV alternative for RMI flows, we now shift our focus to experimental results. From ACCIV velocity field output from experimental data, velocity PDFs are generated and compared in Fig. 8. Noting a nearly Gaussian distribution of velocity, a normal distribution was fit to the data and a standard deviation of 3.26 m/s was found for the transverse velocity, and 4.73 m/s was found for the streamwise component. The mean flow in the streamwise direction was

subtracted off for comparison with flow in the transverse direction, leaving fluctuations around a peak at zero velocity for both components. PDFs of the experimental data show that approximately 99 % of the spanwise and streamwise velocity lies between ± 8.5 and ± 12.4 m/s, respectively. This shows reasonable agreement with the spanwise velocity component shown by Balakumar et al. (2008), though we note a broader distribution of streamwise velocity fluctuations as compared to the transverse, suggesting a more anisotropic flow.

Measurements of anisotropy were also made both across and through the 5–95 % concentration region of the mixing layer. Figure 9 shows the ratio of the transverse to streamwise RMS velocity. A mean value of 0.79 across the mixing layer and 0.65 through the mixing layer, each with fluctuations both above and below 1, indicate that while the streamwise and transverse components of velocity are nearly balanced, neither component is universally dominant within the mixing layer. This anisotropy measurement has been predicted by simulations, but has not previously been measured in experiments. Using the scaling described by Lombardini et al. (2012):

$$t* = \left(\frac{\Delta u}{a_0}\right)^{-1/2} (k_0 A^+ \Delta u) t$$

where Δu is the change in interface velocity induced by the shock, a_0 is the sound speed of unshocked heavy gas, k_0 is the dominant wavenumber, A^+ is the Atwood number, and t is time. We obtain a dimensionless time of $t^* = 150$ for our experimental data and find that our ratio of streamwise to transverse Reynolds numbers is in close agreement at a value of 1.9. In comparison with the work of Thornber et al. (2010), we find that our ratio of fluctuating velocities puts our experimental work at a dimensionless time of 30 based on Thornber et al.'s (2010) definition. Both the aforementioned studies suggest that our flow has not quite yet reached the equilibrium between the streamwise and transverse RMS kinetic energy production terms.

With the RMS velocity determined from ACCIV results, the Taylor Reynolds number of the flow can be found by first calculating the Taylor microscale. This is done by computing the curvature of the autocorrelation curve of the scalar field at $r = 0$ by fitting a parabola to the central seven points, that is, the $r = 0$ point, the next three points, and the equivalent three points on the negative r side of the correlation. A Taylor microscale of $\lambda = 4.2$ mm is found for experimental data. Along with $\nu = 1.6\text{e}{-5}$ m^2/s, this gives a Taylor Reynolds number of approximately $Re_\lambda = \langle u^2 \rangle^{1/2} \lambda / \nu = 855$, which is over the turbulent transition (Dimotakis 2000). Using the relation $Re = (3/20)^* Re_\lambda^2$ (Pope 2000), we find a Reynolds number of 1.1e5, which is slightly higher than might be expected for the flow (Weber et al. 2014). This may be due to the fact that ACCIV returns velocity values only inside the mixing layer, masking the lower velocity outside of it; this would lead to a higher than expected RMS velocity, thus increasing the Reynolds number.

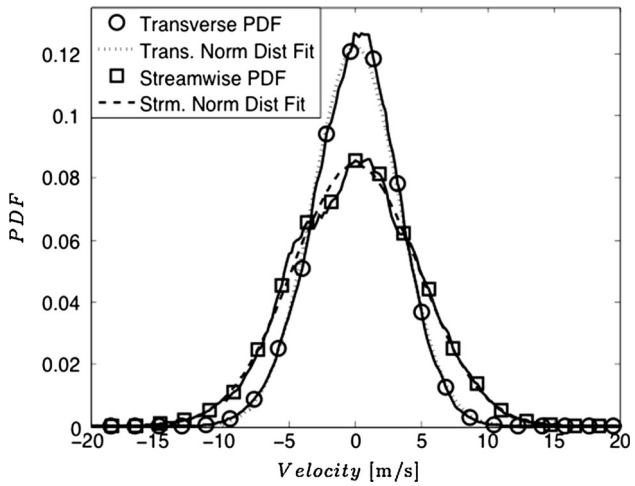

Fig. 8 PDFs of velocity field from experiment

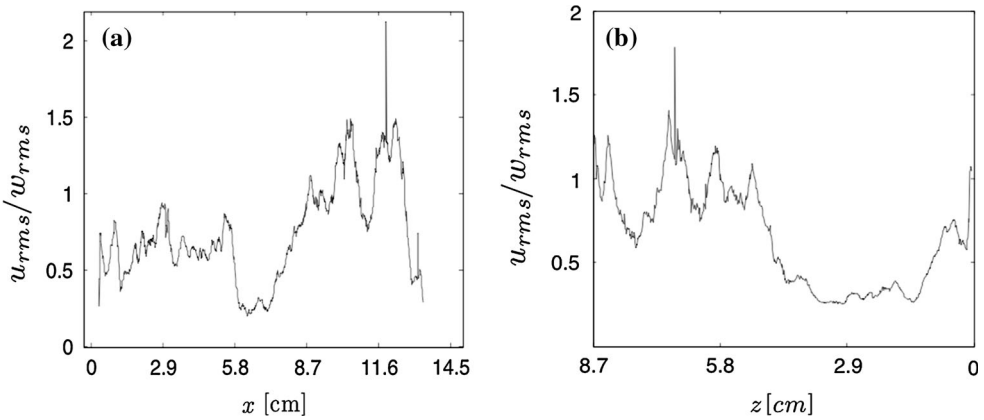

Fig. 9 Ratio of u/w RMS velocities within the mixing layer in the **a** transverse **b** streamwise direction

6 Conclusions

This work presents the first velocity field measurements made in the mixing layer of shock-induced RMI flow using the ACCIV technique. Results show that the flow appears to not have quite reached equilibrium between production of kinetic energy in the streamwise and transverse direction. We find good agreement with simulation and see that ACCIV is able to both return a large number of vectors and give correct values where it is able to detect velocity. The ACCIV technique also has potential to return much higher resolution than PIV methods. While the main drawback of the ACCIV technique is the absence of located vectors in uniform scalar regions of experimental data, these flaws must be weighed against the limitations associated with PIV for a particular setup. A comparison with traditional experimental PIV methods will be studied further in a following paper.

Acknowledgments The authors would like to thank Dr. Xylar Asay-Davis for his valuable correspondence and assistance with the ACCIV software. This research was partially supported by US Department of Energy Grant DE-FG52-06NA26196.

References

Anderson M, Puranik B, Oakley J, Bonazza R (2000) Shock tube investigation of hydrodynamic issues related to inertial confinement fusion. Shock Waves 10:377–387

Arnett D (2000) The role of mixing in astrophysics. Astrophys J Suppl Ser 127(2):213–217

Asay-Davis X, Marcus PS, Wong MH, dePater I (2009) Jupiter's shrinking Great Red Spot and steady Oval BA: velocity measurements with the 'Advection Corrected Correlation Image Velocimetry' automated cloud tracking Method. Icarus 203:164–188

Balakumar BJ, Orlicz GC, Tomkins CD, Prestridge KP (2008) Simultaneous particle-image velocimetry–planar laser-induced fluorescence measurements of Richtmyer-Meshkov instability growth in a gas curtain with and without reshock. Phys Fluids 20:124103

Brouillette M, Sturtevant B (1994) Experiments on the Richtmyer-Meshkov instability: single-scale perturbations on a continuous interface. J Fluid Mech 263:271–292

Cook AW (2007) Artificial fluid properties for large-eddy simulation of compressible turbulent mixing. Phys Fluids 19:055103

Dimotakis PE (2000) The mixing transition in turbulent flows. J Fluid Mech 409:69–98

Lombardini M, Pullin DI, Meiron DI (2012) Transition to turbulence in shock-driven mixing: a Mach number study. J Fluid Mech 690:203–226

Ma T et al (2013) Onset of hydrodynamic mix in high-velocity, highly compressed inertial confinement fusion implosions. Phys Rev Lett 111:085004

Meshkov EE (1970) Instability of a shock wave accelerated interface between two gases. NASA Tech Transl 13:1–14

Olson B, Greenough J (2014) Large eddy simulation requirements for the Richtmyer-Meshkov instability. Phys Fluids 26:044103

Pope SB (2000) Turbulent flows. Cambridge University Press, Cambridge

Prestridge K, Rightley PM, Vorobieff P, Benjamin RF, Kurnit NA (2000) Simultaneous density-field visualization and PIV of a Shock-accelerated Gas Curtain. Exp Fluids 29:339–346

Richtmyer RD (1960) Taylor instability in shock acceleration of compressible fluids. Commun Pure Appl Math 13:297–319

Taylor ZJ, Gurka R, Kopp GA, Liberzon A (2010) Long-duration time-resolved PIV to study unsteady Aerodynamics. IEEE Trans Instrum Meas 59(12):3262–3269

Thornber B, Drikakis D, Youngs DL, Williams RJR (2010) The influence of initial conditions on turbulent mixing due to Richtmyer-Meshkov instability. J Fluid Mech 654:99–139

Tokumaru PT, Dimotakis PE (1995) Image correlation velocimetry. Exp Fluids 19(1):1–15

Vorobieff P, Anderson M, Conroy J, White R, Truman CR, Kumar S (2011) Vortex formation in shock accelerated gas induced by particle seeding. Phys Rev Lett 106:184503-1–184503-4

Weber C. (2012) Turbulent Mixing Measurements in the Richtmyer-Meshkov Instability (Doctoral dissertation, University of Wisconsin-Madison). Available from ProQuest Dissertations and Thesis database. (UMI no. 3548185)

Weber C, Haehn N, Oakley J, Rothamer D, Bonazza R (2012) Turbulent mixing measurements in the Richtmyer–Meshkov instability. Phys. of Fluids 24:074105

Weber C, Cook A, Bonazza R (2013) Growth rate of a shocked mixing layer with known initial perturbations. J Fluid Mech 725:372–401

Weber C, Haehn N, Oakley J, Rothamer D, Bonazza R (2014) An experimental investigation of the turbulent mixing transition in the Richtmyer-Meshkov instability. J Fluid Mech 784:457–487

Westerweel J, Elsinga GE, Adrian RJ (2013) Particle image velocimetry for complex and turbulent flows. Annu Rev Fluid Mech 45:409–436